Karazin Kharkiv National University
Department of Physics and Technology

Technische Universität Darmstadt
Institut für Kernphysik

Dipole Strength in ^{112}Sn up to 7 MeV from a Nuclear Resonance Fluorescence Study at the S-DALINAC

Diploma Thesis

Iryna Poltoratska

Darmstadt

February 2005

Abstract

An investigation of low-lying electric dipole excitations in the semi-magic nuclide ^{112}Sn with the help of nuclear resonance fluorescence is presented in the following work. The experimental data were obtained at the superconducting Darmstadt electron linear accelerator S-DALINAC using bremsstrahlung with endpoint energies 5.5 MeV, 7 MeV and 9.5 MeV. Data obtained for excitation energies of 5.5 MeV and 7 MeV were analyzed in this work.
The excitation energies and the ground state transition widths are determined for the data. All about 30 newly observed states show dipole character. A detailed picture of the fine structure of the dipole strength in ^{112}Sn is observed. The strong fragmentation of the dipole strength is found in the excitation energy region of 6 MeV to 7 MeV. It can be interpreted as part of the electric Pygmy dipole resonance. The extracted total E1 transition strength in the range for excitation energies up to 6.5 MeV amounts to $\sum$B(E1)$\uparrow$=0.089 e^2fm^2 with a centroid energy E$_x$=6.14 MeV.

Contents

1 Introduction **1**

2 Nuclear Resonance Fluorescence **5**

2.1 Scattering Cross Section 6

2.2 Transition Width and Reduced Transition Strength 8

2.3 Angular Distribution 10

3 Experimental Procedure **13**

3.1 S-DALINAC and Experimental Facilities 13

3.2 Experimental Setup 14

3.3 HPGe Detectors 17

3.4 BGO Shield 19

3.5 Data Acquisition 21

3.6 Experimental Details 22

4 Analysis and Results **23**

4.1 Energy Calibration 23

4.2 Experimental Angular Distributions 23

4.3 Detector Efficiency 26

4.4 Photon Flux and Extraction of Integrated Cross Sections . . . 29

4.5 Results 32

5 Discussion **36**

6 Concluding Remarks **39**

References **40**

1 Introduction

The investigation of the strong electric dipole excitations has been a major field of nuclear structure in recent years. One can schematically divide such excitations into three groups which are indicated in Fig. 1.

Probably the most famous (and also the strongest) excitation mode is the so-

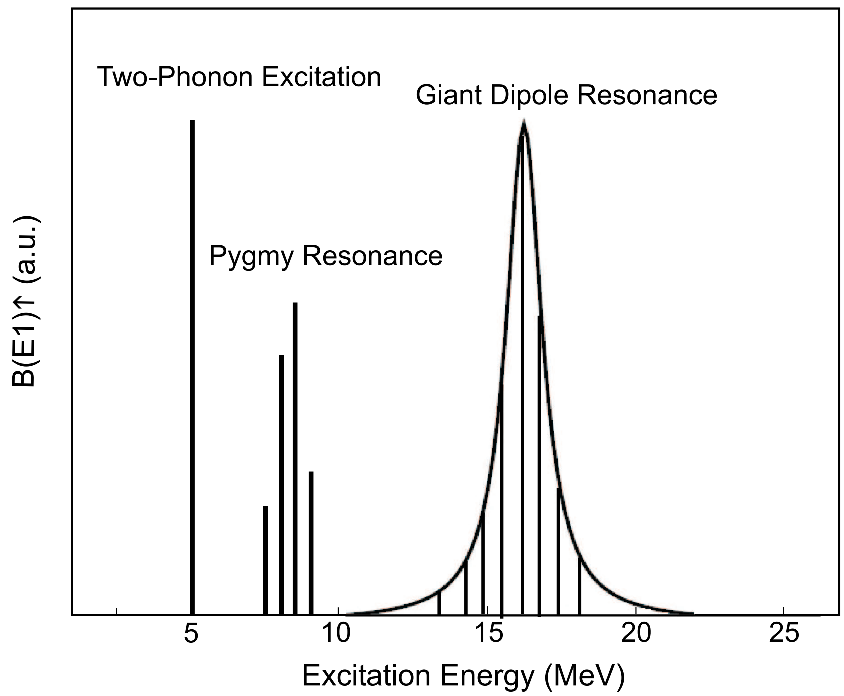

Figure 1: Schematic overview of the B(E1) strength distribution in nuclei.

called electric giant dipole resonance (GDR), which lies at energies between 10 and 20 MeV and forms a broad structure. It's well studied since many years [1] and can be interpreted as out-of-phase oscillations of protons versus neutrons, thus inducing a dynamical electric dipole moment. Due to the repulsive nature of the particle-hole (p-h) interaction, the major part of the total E1 strength is concentrated at high excitation energies. The centroid of the excitation strength of such oscillations lies in heavy nuclei approximately at an energy [2]

$$E_x \;=\; 79\; A^{-\frac{1}{3}}\;\mathrm{MeV}. \tag{1}$$

In ^{112}Sn it is located around 16.3 MeV. The experimentally observed dipole strength of the GDR exhausts almost 100% of expected total dipole strength, which can be estimated with the help of Thomas-Reiche-Kuhn energy-weighted sum rule (EWSR), giving the total integration cross section for electric dipole photon absorption in the absence of exchange forces

$$\mathrm{EWSR} \;=\; 60\;\frac{NZ}{A}\;\mathrm{mb\;MeV}. \tag{2}$$

Furthermore one observes a single strong isolated electric dipole excitation at lower energy which is interpreted as a member of a quintuplets of states which originate from the coupling of 2^+ and 3^- phonons [3, 4]. Phonons are oscillation modes in nuclei. If one couples a 2^+ quadrupole-phonon with 3^- octupole-phonon, one receives a quintuplet of states with J^π=1^-,..,5^-. One can prove the two-phonon character of these states unambiguously by investigating their excitation and decay behavior.

Low-energy electric-dipole resonances are a topic of high current interest, caused by significant experimental progress in studies of its properties in stable as well as exotic, neutron-rich nuclei. In stable nuclei they have been known for a long time [5], but their nature and systematic features remained poorly understood. A wide range of models of these modes usually called pygmy dipole resonance (PDR) has been discussed (for a list of references,

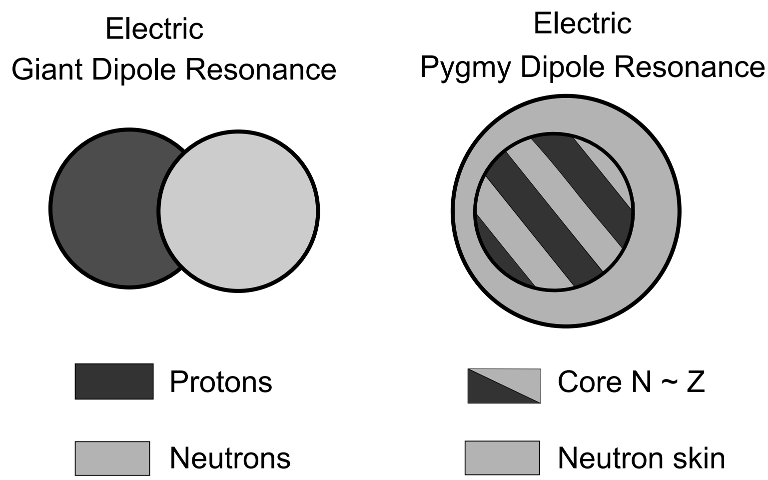

Figure 2: Dipole excitations in nuclei.

see [6]). Recent experimental progress has been achieved by detailed measurements of low-lying $E1$ strength and its fine structure at $Z = 20$ [7] and $N = 82$ [8] shell closures, as well as for the doubly magic ^{208}Pb [9, 10] using the nuclear resonance fluorescence (NRF) technique [11]. Strongly excited soft $E1$ modes have also been observed recently in exotic, very neutron-rich isotopes [12, 13, 14]. These are mostly believed to result from oscillations of the excess neutrons against an stable proton/neutron core with N $\sim$ Z. It is certainly an interesting question whether the low-lying $E1$ strength in nuclei close to the valley of stability, although certainly less pronounced, is generated by the same mechanisms or whether the structural features change for extreme neutron-to-proton ratios.

The Sn isotopes are interesting because of recent microscopic predictions which differ considerably. One shows a smooth increasing of the total B(E1) strength with the N/Z ratio and expects maximum of it at ^{120}Sn [15, 16, 17]. A systematic experimental study of the dipole strength in even-mass Sn isotopes with mass numbers 116 up to 124 using the (γ, γ') reaction has been recently reported [18, 19, 20]. To further explore the systematics a NRF experiment on ^{112}Sn was carried out at the S-DALINAC. Because of the low natural abundance, data on excited states in ^{112}Sn are scarce [21]. The motivation of the present experiment was mainly a search for a low-lying dipole strength in ^{112}Sn addressing the problem of the PDR with high sensitivity.

2 Nuclear Resonance Fluorescence

The NRF method represents an outstanding tool to investigate low-spin states excited via dipole and quadrupole transitions from the ground state [11, 22]. The specific spin selectivity and low detection limit of this probe allow to study even weak dipole and quadrupole excitations at excitation energies where the total level density is already rather high [23].

For NRF experiments one usually uses bremsstrahlung, which can be produced by decelerating electrons. Photons with resonant energy will excite a target nucleus with a certain probability into a state with excitation energy E_x, spin-parity J^π and lifetime Γ (see Fig. 3). After some *fs* to *ps* the excited nuclei will decay either back to the ground state (elastic transition with decay width Γ_0) or to some other lower-lying excited states (inelastic transitions with J_i^π and Γ_i).

Evaluating the data obtained from a NRF experiment it is possible to deter-

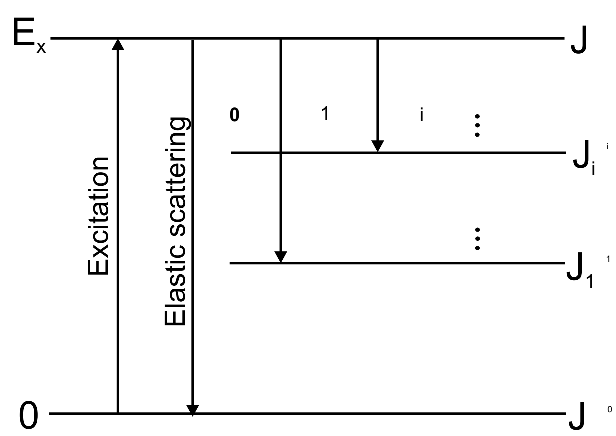

Figure 3: Gamma transitions in nuclear resonance fluorescence.

mine in model-independent way a large set of quantities characterizing the excited state

- excitation energy,
- spin and parity (if a primary polarized gamma beam is available or a Compton polarimeter is used),
- ground state decay width,
- lifetime,
- transition strength.

2.1 Scattering Cross Section

The cross section of the NRF process has a resonant shape described by a Breit-Wigner distribution

$$\sigma_f^0(E) \;=\; \frac{\pi}{2} \cdot \left(\frac{\hbar c}{E_x}\right)^2 \cdot g \cdot \frac{\Gamma_0 \Gamma_i}{(E_\gamma - E_x)^2 + \frac{\Gamma^2}{4}}, \tag{3}$$

where E_γ is the energy of the incoming photon, Γ is the total decay width of the resonant state with energy E_x, Γ_i is the partial width for photon decay to the state i ($i = 0$ denotes the ground state), and g is a statistical factor which depends upon the ground state total angular momentum J_0 and the angular momentum of the excited level J

$$g = \frac{2J+1}{2J_0+1}. \tag{4}$$

The total decay width Γ is connected to the lifetime τ of the excited level via the uncertainty relation

$$\Gamma \;=\; \sum_i \Gamma_i \;=\; \frac{\hbar}{\tau}. \tag{5}$$

The total cross section is given by the sum of the partial cross sections of decays to all possible final states

$$\sigma^{total}\left(E_{\gamma}\right) = \sum_{i} \sigma^{i}\left(E_{\gamma}\right) = \frac{\pi}{2} \cdot \left(\frac{\hbar c}{E_{x}}\right)^{2} \cdot g \cdot \frac{\Gamma_{0}\Gamma}{\left(E_{\gamma} - E_{x}\right)^{2} + \frac{\Gamma^{2}}{4}}. \tag{6}$$

If a primary photon with energy E_{γ} is absorbed by a nucleus which is initially at rest and in a ground state, then, because of the finite mass of the nucleus, a part of the energy ΔE_{rec} is transferred to the nucleus as a recoil, so that $E_{x} = E_{\gamma} + \Delta E_{rec}$, with

$$\Delta E_{rec} = \frac{E_{\gamma}^{2}}{2Mc^{2}}, \tag{7}$$

where M is the rest mass of the emitting nucleus. The excited nucleus is moving in the direction of the primary gamma beam. If during the short decay time to the ground state a secondary photon is emitted, its energy will experience a Doppler shift in addition to the recoil correction. Thus, the emitted photon will have a different energy dependence on the emission angle θ with respect to the incoming γ-quantum, which excites the nucleus

$$E_{\gamma} = E_{x} - \frac{E_{\gamma}^{2}}{2Mc^{2}} \cdot [1 - 2\cos\theta]. \tag{8}$$

If this energy difference is larger than the width of the level, as is generally the case, then the cross section for resonance absorption of the emitted photon by neighbouring nuclei in a monoisotopic target becomes extremely small. This is a precondition to make the detection of emitted gammas with the NRF method possible at all.

Another important factor for NRF experiments is the thermal motion of atoms in the target. This motion causes a Doppler broadening of the absorption line width, which is generally several orders of magnitude larger than the natural width of the emission and absorption lines. It can be assumed that the thermal velocities of nuclei v have a Maxwellian distribution [24]

$$f(v) = \left(\frac{M}{2\pi kT}\right)^{\frac{1}{2}} \exp\left(-\frac{Mv^2}{2kT}\right), \tag{9}$$

where M is the nuclear mass, k is the Bolzmann constant, and T is the absolute temperature. Then instead of Eq. (3) one obtains the Doppler-broadened Breit-Wigner distribution

$$\sigma^i_{DBW}(E_\gamma, T) = 2\pi \cdot \left(\frac{\hbar c}{E_x}\right)^2 \cdot g \cdot \frac{\Gamma_0}{\Gamma} \cdot \frac{\Gamma_i\sqrt{\pi}}{2\Delta} \exp\left[-\left(\frac{E_\gamma - E_x}{\Delta}\right)^2\right], \tag{10}$$

where Δ is the Doppler width

$$\Delta = E\sqrt{\frac{2k_BT}{Mc^2}}. \tag{11}$$

Since the energy resolution of High Purity Germanium (HPGe) detectors widely used for the detection of the emitted photons is usually worse than the Doppler broadening of line width, one practically measures the integrated cross section I_i which can be deduced by integration of Eq. (10) over the entire range of photon energies

$$I_i = \int \sigma^i_{DBW}(E_\gamma, T)\, dE_\gamma = \pi^2 \cdot \left(\frac{\hbar c}{E_x}\right)^2 \cdot g \cdot \frac{\Gamma_0\Gamma_i}{\Gamma}. \tag{12}$$

In the case of elastic transitions ($\Gamma_i = \Gamma_0$) we have

$$I_0 = \pi^2 \cdot \left(\frac{\hbar c}{E_x}\right)^2 \cdot g \cdot \frac{\Gamma_0^2}{\Gamma}. \tag{13}$$

2.2 Transition Width and Reduced Transition Strength

Electromagnetic transitions are characterized by the multipolarity λ with $\lambda = 0, 1, 2, ...$ for monopole, dipole, quadrupole *etc.* There exists a selection rule for allowed electromagnetic transitions relating the spins of the initial and final states J_i and J_f with the multipolarity of the transition from these two states

$$|J_i - J_f| \leq \lambda \leq J_i + J_f. \tag{14}$$

The parities of these states define the type of the transition:

$$\pi_i = (-1)^{\lambda} \cdot \pi_f \qquad \text{for electric transitions,} \tag{15}$$

$$\pi_i = (-1)^{\lambda+1} \cdot \pi_f \qquad \text{for magnetic transitions.} \tag{16}$$

The ground state decay width Γ_0 is proportional to the reduced transition probability $B(\Pi\lambda, E_\gamma)\uparrow$

$$\Gamma_0 = 8\pi \sum_{\Pi\lambda=1}^{\infty} \frac{(\lambda+1)}{\lambda\left[(2\lambda+1)!!\right]^2} \cdot \left(\frac{E_\gamma}{\hbar c}\right)^{2\lambda+1} \cdot \frac{2J_0+1}{2J+1} \cdot B\left(\Pi\lambda, E_\gamma\right)\uparrow, \tag{17}$$

where $\Pi = E$ for electric transitions and $\Pi = M$ for magnetic ones. The photon can transfer only a small momentum to a nucleus. Therefore, in NRF experiments one excites mostly dipole transitions and to a lesser extent quadrupole transitions.

For even-even nuclei one has the following relations between reduced transition strengths and ground state decay widths

$$\frac{B(E1)\uparrow}{[\mathrm{e}^2\mathrm{fm}^2]} = 9.554 \cdot 10^{-4} \cdot g \cdot \frac{\Gamma_0}{[\mathrm{meV}]} \cdot \left(\frac{[\mathrm{MeV}]}{E_x}\right)^3, \tag{18}$$

$$\frac{B(M1)\uparrow}{[\mu_N^2]} = 8.641 \cdot 10^{-2} \cdot g \cdot \frac{\Gamma_0}{[\mathrm{meV}]} \cdot \left(\frac{[\mathrm{MeV}]}{E_x}\right)^3, \tag{19}$$

$$\frac{B(E2)\uparrow}{[\mathrm{e^2fm^4}]} \;=\; 1.245\cdot 10^3\cdot g\cdot\frac{\Gamma_0}{[\mathrm{meV}]}\cdot\left(\frac{[\mathrm{MeV}]}{E_x}\right)^5. \tag{20}$$

The reduced transition probabilities $B(\Pi\lambda;\mathrm{J}\rightarrow J_0)$=B($\Pi\lambda$)$\downarrow$ and $B(\Pi\lambda;\mathrm{J_0}\rightarrow\mathrm{J})$=B($\Pi\lambda$)$\uparrow$ differ by the statistical factor introduced in Eq. (4)

$$B\left(\Pi\lambda\right)\uparrow=\frac{2J+1}{2J_0+1}\cdot B\left(\Pi\lambda\right)\downarrow. \tag{21}$$

2.3 Angular Distribution

By measuring the angular distribution of the emitted photons with respect to the incident beam in a NRF experiment, the multipole order (dipole or quadrupole) of a transition can be determined [22]. The angular distribution function $W(\theta)$ for resonantly scattered real photons is given by the following expression

$$W\left(\theta\right)=\sum_{\nu=0,2,4,...}A_\nu^{i\rightarrow j}\cdot A_\nu^{j\rightarrow k}P_\nu\left(\cos\theta\right), \tag{22}$$

where θ is the angle between scattered and primary photon and $P(\cos\theta)$ are Legendre polynomials. The coefficient $A_\nu^{i\rightarrow j}$ describes the photon in the entrance channel, and similarly $A_\nu^{j\rightarrow k}$ takes into account the resonantly scattered photon.

Even-even nuclei always have ground state angular momentum and the parity $J_0^\pi=0^+$. As a consequence, only levels with spin 1 or 2 can be excited in (γ,γ') experiments on even-even targets. In the case of elastic scattering, only the spin sequences $0-1-0$ and $0-2-0$ will occur, corresponding to pure dipole and quadrupole transitions, and the following expressions for the

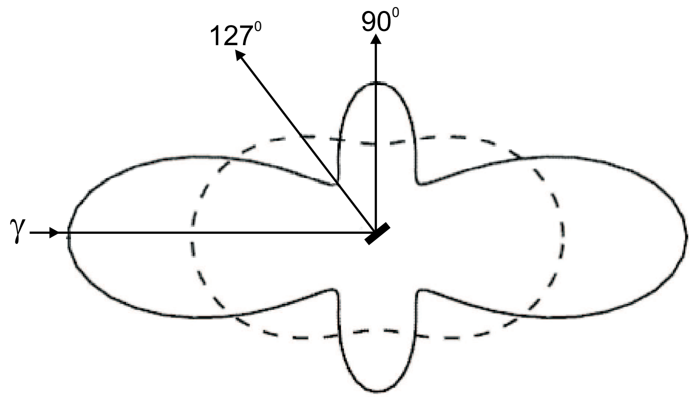

Figure 4: Angular correlations for dipole ($0-1-0$, dashed curve) and quadrupole ($0-2-0$, solid curve) transitions.

angular distribution functions $W(\theta)$ are obtained [25]

$$W\left(\theta\right)_{Dipole} = \frac{3}{4} \cdot \left(1 + \cos^2\theta\right), \tag{23}$$

$$W\left(\theta\right)_{Quadrupole} = \frac{5}{4} \cdot \left(1 - 3\cos^2\theta + 4\cos^4\theta\right). \tag{24}$$

These angular distribution functions are plotted in Fig. 4. From this figure one can see that the angular distribution for dipole transitions at 90° has a minimum whereas for quadrupole transitions it has a maximum at 90° and two minima at 53° and 127°. The angle 127° is more favorable than 53° for a NRF experiment due to the dramatic background decrease at backward angles (because of the dominance of atomic scattering at forward angles), so the best distinction between the two distributions exists at the scattering angles of 90° and 127°. The intensity ratio $W(90°)/W(127°)$ is 0.73 for dipole and 2.28 for quadrupole transitions, respectively. For comparison with experiment, these values need to be corrected for the actual geometry (slightly deviating angles, opening angles of detectors, etc.) Furthermore, they may be modified by feeding of the lower-lying levels from higher-lying excited states.

3 Experimental Procedure

3.1 S-DALINAC and Experimental Facilities

The present experiment was performed at the superconducting Darmstadt electron linear accelerator S-DALINAC [26] at the Institute for Nuclear Physics of the Darmstadt University of Technology. It became the first superconducting continuous-wave linear accelerator of electrons in Europe. Since 1991, the S-DALINAC delivers electron beams with a maximum energy of 130 MeV and currents up to 50 μA for a wide range of nuclear physics experiments. The layout of the accelerator is shown in Fig. 5.

The electrons are emitted by a cathode and then accelerated electrostati-

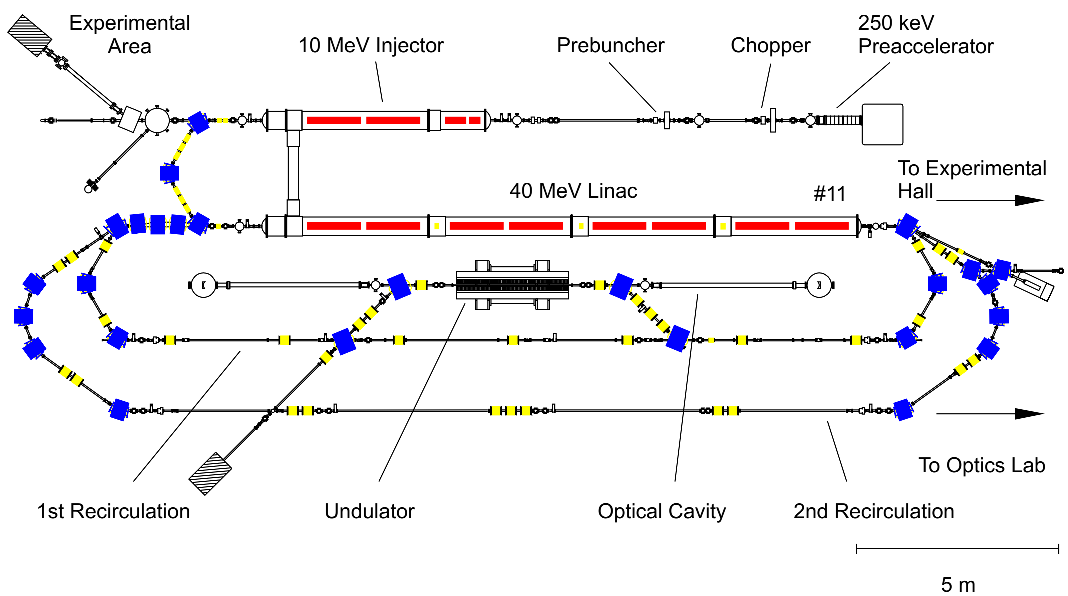

Figure 5: Schematic layout of the S-DALINAC.

cally to an energy of 250 keV. The required time structure of the electron beam for radio-frequency acceleration in a 3 GHz field is prepared by a chopper/prebuncher system operating at room temperature. The superconducting injector linac consists of one 2-cell, one 5-cell, and two standard 20-cell niobium structures, cooled to temperature of a 2 K by liquid helium. Leaving the injector, the beam has an energy of up 10 MeV and can either be used for radiation physics experiments or for nuclear resonance fluorescence experiments. Alternatively, it can be bent by 180° and injected into the main accelerator section. This superconducting linac has eight 20-cell cavities which provide an energy gain of up to 40 MeV. After passing through the main linac the electron beam may be extracted towards the experimental hall or it can be reinjected twice into the main linac using two separated recirculating beam transport systems. After three passes the electron beam with an energy of up to 130 MeV is delivered to several experimental facilities, schematically shown on the Fig. 6. A wide range of electron scattering experiments is carried out using the large solid angle and momentum acceptance magnetic spectrometer QCLAM or magnetic spectrometer Lintott, optimized for beam dispersion matching to obtain the highest possible resolution.

3.2 Experimental Setup

In NRF experiments the targets of interest are irradiated by a continuous bremsstrahlung beam, which is produced by decelerating electrons in a massive conversion target, called radiator. The photon beam cone is defined geometrically by means of a collimator behind the radiator. The NRF facility at the S-DALINAC [27] is shown in Fig. 7. In the present setup a

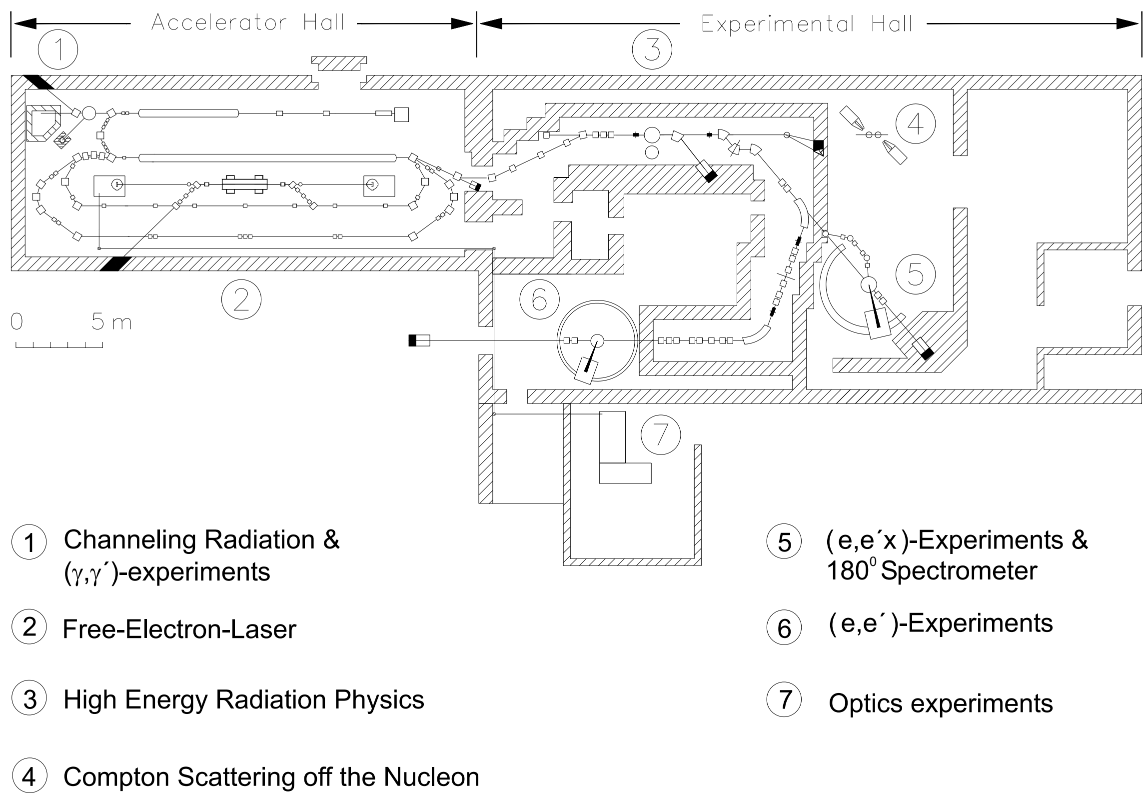

Figure 6: Schematic layout of the S-DALINAC and its experimental areas.

relatively close geometry between radiator, target and detectors has been realized to obtain a high photon flux. The distance between the radiator and the target for the photon scattering experiments (NRF target) is about 1.5 m. The photon flux is monitored by an ionization chamber located about 1 m behind the NRF target. Scattered photons are detected by high purity Germanium (HPGe) crystal detectors having an efficiency of photopeak conversion of 100% relative to a 3″ × 3″ standard NaI detector. The detectors were positioned at 90° and 130° with respect to the direction of the incoming photon flux.

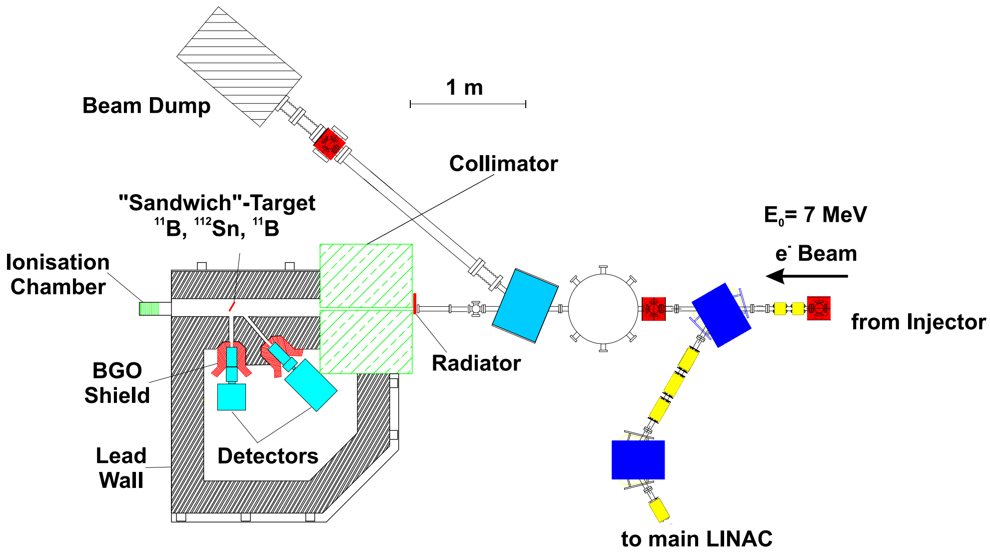

Figure 7: Schematic layout of the NRF setup at the S-DALINAC.

A 14 mm thick copper radiator [28] is used to produce neutron-free continuous γ-spectra with energies up to 10 MeV. The requirements for any radiator material are a high heat conductivity and a high melting point to avoid the melting of the radiator. The radiator is additionally cooled by an air fan.

The maximum energy of the photons, which can be achieved by the injector at the S-DALINAC is about 10 MeV. Therefore, in order to decrease the background from neutrons produced in (γ,n) reactions one has to use a material for the photon collimator and radiator with neutron separation energies $\gtrapprox$ 10 MeV for all stable isotopes. For these considerations copper is chosen with neutron separation energies $S_n = 9.91$ MeV and $S_n = 10.9$ MeV for two existent stable isotopes ^{63}Cu and ^{65}Cu, respectively. The collimator hole has a conical shape, changing from a diameter of 12 mm at the entrance to 20 mm at the exit. Additional copper bricks are arranged around the collimator on the radiator side. Because the bremsstrahlung is emitted mainly in forward direction, this setup avoids neutron-induced background from the collimator. The remaining area between the radiator and the detectors is filled with iron and lead to reduce the γ-ray flux at the detector positions.

3.3 HPGe Detectors

The detectors used in the present experiment were of HPGe type. The high purity germanium (HPGe) detector is a semiconductor detector based on a reverse biased p-n junction. It has a density of impurities of less than 10^{10} atoms/cm^3, compared with 10^{12} atoms/cm^3 for normal semiconductors [29]. The HPGe crystal purity is not affected by temperature, allowing storage without cooling, but due to the small band gap of germanium (0.7 eV) they must be cooled to liquid nitrogen temperature (77 K) in order to reduce thermal noise during the operation. For gamma-ray spectroscopy, an active volume as large as possible is required, so the detectors are constructed in a bulletized coaxial shape.

The photon entering the Ge crystal loses its energy, producing particle-hole pairs in the semiconductor. This is realized via the processes of Compton effect, photoeffect, and pair production. The charge produced is proportional to the energy deposited by the photon in the crystal. The energy required to form an electron-hole pair in HPGe detectors is about 3 eV which may be compared to typical ionisation energies required in gas detectors and scintillators of about 30 keV. This has two consequences: first, there is a small statistical fluctuation in the number of charge carriers per pulse, and second, as a result of the large number there is an excellent signal to noise ratio, both leading to a good energy resolution.

For the detection of the emitted gamma radiation two HPGe detectors were used in the present experiment positioned distances of 26 cm and 26.5 cm, respectively. The first detector was positioned at 90° with respect to the primary beam axis. Further on it will be called "Compton-Polarimeter", or simply "Polarimeter" [31] because of its segmented structure which allows - in principle - parity determination via the Compton effect in a double scattering experiment. However, this requires extremely high statistics and the feature is not used in the present work. The second detector, called "Detector", was positioned at an angle of 130°. Parameters of these two detectors are given in Tab. 1. The detectors were surrounded

Table 1: Detectors Parameters

Detector angle	90°	130°
Crystal volume	362 cm^3	375.7 cm^3
Operating voltage	+4.5 kV	-5.0 kV
Relative efficiency[a]	100%	100%
Energy resolution at 1332 keV	2.4 keV	2.2 keV

[a]relative to $3'' \times 3''$ NaI(Tl)-Crystall at 1332 keV

by massive lead walls (more than 10 cm thick) in order to shield them against gamma radiation from the accelerator. Only from the target side openings with a diameter of 5 cm exist. In front of each detector thin copper bricks were placed to suppress low-energy background from the target.

3.4 BGO Shield

For the detection of the photon it is desirable that it looses all its energy in the crystal. Those events, in which only a part of the photon energy is deposited in the crystal, do not contribute to the photopeak but only to the background. In order to suppress such events, a BGO shield was used [30, 31]. It is a detector based on an inorganic bismuth germanate scintillator ($Bi_4Ge_3O_2$). The large atomic number of bismuth (Z=83) and its high density (7.3 g/cm^2) make BGO ideal for the detection of γ rays. In comparison with NaI, another commonly used scintillator, 6 cm of BGO is required to absorb a 1 MeV γ ray, whereas 14 cm would be required for NaI. However, BGO has a light yield of $\approx$15% of NaI [32]. Therefore, BGO is used when the need for high γ-ray counting efficiency outweighs the need for energy resolution. This scintillator has a much lower energy resolution in comparison with the HPGe-detector, but the detection efficiency is also 100% relative to the NaI crystal. An electronic anticoincidence between the signal from the main HPGe crystal and the BGO-shield was set up. All those events in which a signal was simultaneously registered by the detector and by the BGO shield were treated as background and were ignored.

Besides Compton-scattered γ-quanta also events from cosmic rays contribute to the background in the spectrum. These events can also be suppressed by the BGO shield. Moreover by use of a BGO single-escape (SE) and double-escape (DE) lines are reduced significantly. The advantage of such an active shielding is demonstrated in Fig. 8.

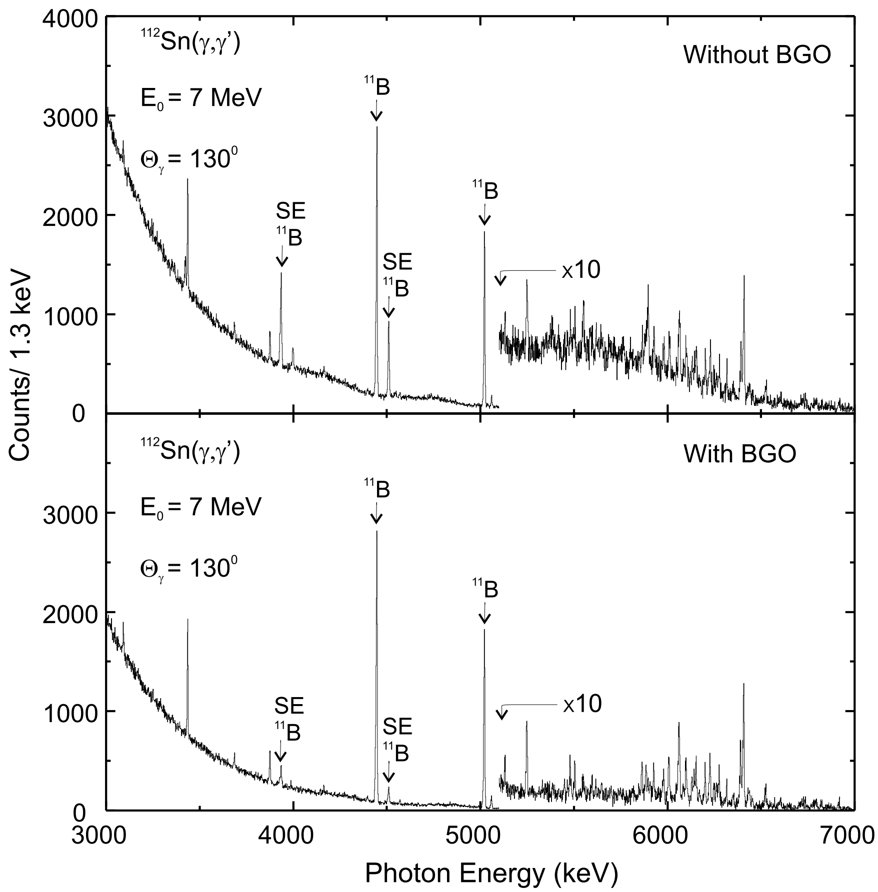

Figure 8: Spectra detected at 130° with and without BGO shield.

3.5 Data Acquisition

Modern nuclear resonance fluorescence experiments are possible only by the application of the extensive electronics. The NIM and CAMAC standards that allow the exchange of components of different manufacturers are used. The detector signals of the single crystal segments are amplified in the preamplifier of the detector. For a better time resolution one gives the signal at first on a Quad-TFA (Quad-Timing-Filter-Amplifier). For the energy signal of the Polarimeter cores it is better to use a spectroscopy amplifier. After amplifiers the signal can be given directly on an ADC (Analogue-Digital-Converter), this converts analogous signal into a digital one which is evaluated by the measuring card of the PC [33].

The data are processed at the same time with two different data acquisition systems. With the first system the energy signals from the detectors anticoincide by means of the ADC rejection with signals from the BGO detectors. As a result one has surely sensible to noise, uncomplicated system which can monitor the experiment slightly online. The second data acquisition system which is based on list mode-components admits a detale analysis of the data. In the (γ, γ') experiments this system is used in combination with the Compton-Polarimeter to determine the parity of the observed states [34].

For further data analysis the program WinTMCA is used which sorts events into histograms. Spectra for both detectors with and without BGO suppression is recorded. Each raw spectrum has 8192 channels. A more precise description of the data acquisition can be found in Ref. [31].

3.6 Experimental Details

The experiment was carried out in the spring of 2003. Electrons with an energy of 5.5 MeV, 7 MeV and 9.5 MeV were used to generate bremsstrahlung spectra.

A target made of highly enriched (>99%) ^{112}Sn material having a weight of 1990.5 mg was sandwiched between two thin layers of ^{nat}B with a total weight 1017.15 mg. The well-known transitions in ^{11}B were used for energy calibration of the detectors and also for the photon flux and efficiency determination. In addition, placing Boron targets on the front and the back side of the ^{112}Sn target allowed to correct for the effect of photon flux decrease in the target.

Behind the target an ionization chamber was used for monitoring the photon flux. The beam transport system was optimized to achieve the maximum current in the ionization chamber which corresponded to the maximum of the photon flux on the target.

During the experiment the energy of the electrons and the electron beam quality were periodically controlled deflecting the electron beam by 40° with a dipole magnet and by checking the position and the spatial distribution of the beam spot on a scintillating target with a video camera.

The average electron beam current was 20 μA. The total time of the measurements at 5.5 MeV, 7 MeV and 9.5 MeV was 20, 66 and 72 hours, respectively, but so far only part of the data have been analyzed. As mentioned already above the present thesis deals with the data analysis interpretation of the spectra up to 7 MeV only. The analysis of the data at endpoint energy of 9.5 MeV is presently performed within the thesis of B. Özel [35].

4 Analysis and Results

4.1 Energy Calibration

In order to find the correspondence between the channels and the energy a calibration target is used, for which the energies of γ lines are well known. In present experiment ^{11}B was used. In the calibration procedure the recoil and Doppler corrections of the boron lines were taken into account. The results of such calibration are shown in Fig. 9. Figure 10 shows the energy-calibrated experimental (γ, γ') spectra of ^{112}Sn for the energy region between 3 and 7 MeV.

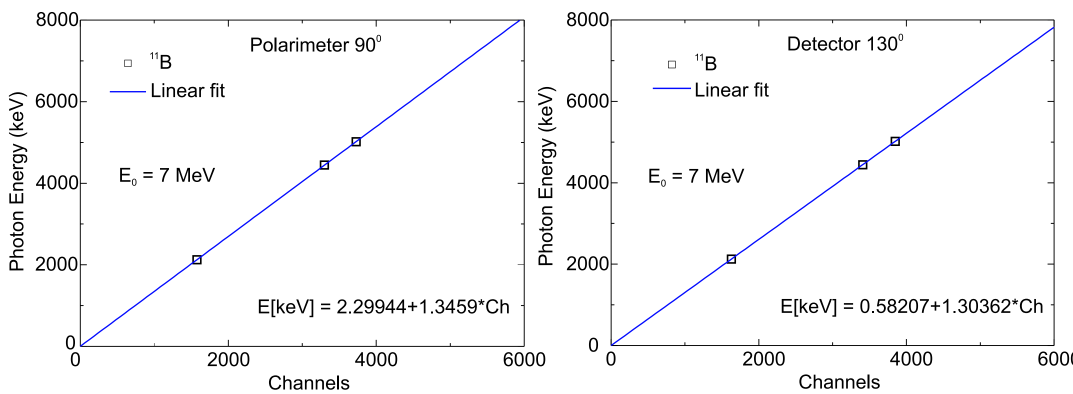

Figure 9: Energy calibration of the detectors using known transitions in ^{11}B.

4.2 Experimental Angular Distributions

The multipolarities of the observed transitions can be extracted from the ratio of the peak intensities measured at different scattering angles [22]. Figure 11 shows these ratios for the 90° and 130° detectors. One can distinguish four

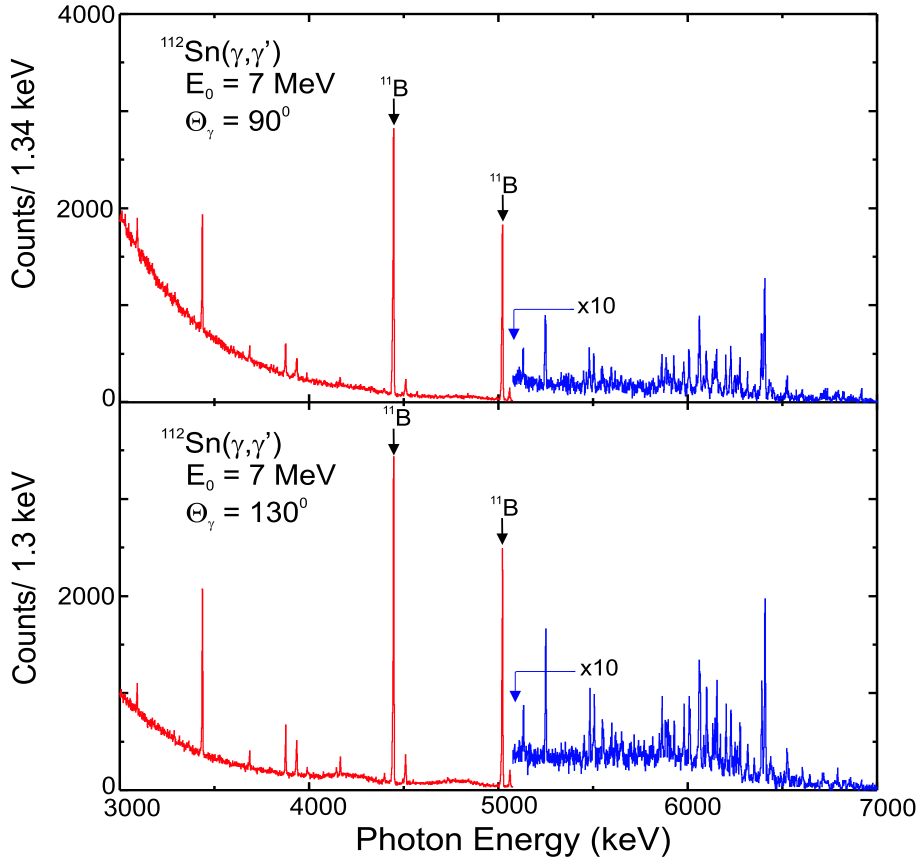

Figure 10: Energy-calibrated spectra at 90° and 130° in the energy region from 3 to 7 MeV.

type of transitions. The open circles and triangle mark known quadrupole transitions [21] and one dipole transition [36], respectively, belonging to ^{112}Sn. Full squares display ^{11}B levels. Full circles mark dipole transitions in ^{112}Sn which were unknown. The solid lines in this figure represent the theoretically predicted ratios of the angular distribution functions $W(90°)/W(130°)$ for dipole $(0-1-0)$ and quadrupole $(0-2-0)$ transitions, corrected for

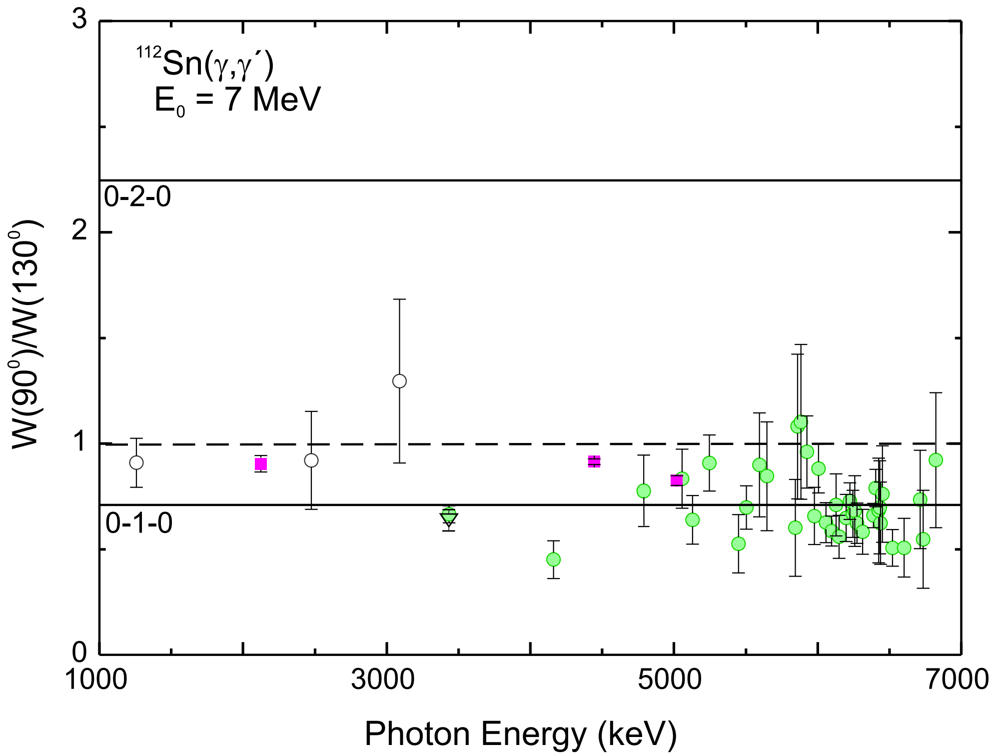

Figure 11: Angular distributions of the transitions excited in the $^{112}\mathrm{Sn}(\gamma, \gamma')$ reaction at $\mathrm{E}_0 = 7$ MeV.

the solid angles of the detectors, while the dashed line indicates an isotopic distribution. The errors are statistical only. All observed ground state transitions above 4 MeV turn out to have a dipole character. The extracted value of the ratios for transitions with $\lambda = 2$ is lower than theoretically predicted because of the strong feeding from levels at high energies. ^{11}B values are close to $W(90°)/W(130°) \approx 1$ [23, 37] because generally odd-spin angular correlations are much more isotopic.

4.3 Detector Efficiency

For the extraction of cross sections one needs the absolute efficiency of the detector. The absolute efficiency is defined as [28]

$$\epsilon_{abs} = \frac{\text{number of detected pulses in the photopeak}}{\text{number of quanta emitted by source}}. \tag{25}$$

Since it depends on the experimental geometry, it is useful to define also an intrinsic efficiency which depends only on the detector properties

$$\epsilon_{ins} = \frac{\text{number of detected pulses in the photopeak}}{\text{number of quanta fallen on detector}}. \tag{26}$$

The energy dependence of the intrinsic efficiency $\varepsilon(E)$ can be determined for each detector from a measurement using radioactive sources. Here, ^{56}Co is used because of its rather high gamma energies. The isotope ^{56}Co undergoes β^+ decay to ^{56}Fe with a half life of 77.3 days. This radioactive source provides 19 gamma transitions with energies between 0.6 and 3.6 MeV with well known relative γ intensities, summarized in Tab. 2. The efficiency can be deduced relative to the strongest transition at 847 keV. The efficiency calibration spectra have been recorded using a ^{56}Co source with the same dimensions as the NRF target placed exactly at the target position. Since only the energy region up to 3.5 MeV is covered by the ^{56}Co, for higher energies Monte Carlo simulations with the computer Code GEANT4 [38] were made. The absolute efficiency as the result of simulations and the measured relative efficiency are shown in Fig. 12 for two detectors.

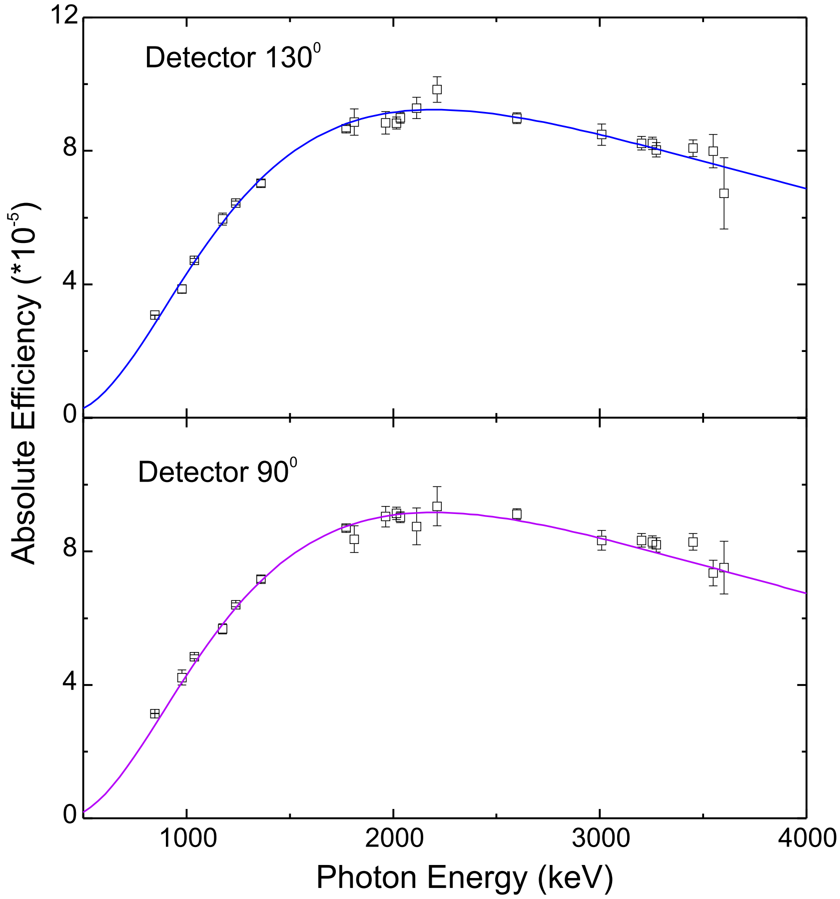

Figure 12: Absolute efficiency for the detector at 130° (upper part) and at 90° (lower part) determined with the help of GEANT4 (line) and the radioactive ^{56}Co source (squares).

Table 2: Gamma transitions of ^{56}Co β-decay with their relative intensities [21].

Energy (keV)	Intensity %
846.771(4)	99.94(3)
977.373(4)	1.449(15)
1037.840(6)	14.17(13)
1175.102(6)	2.288(21)
1238.282(7)	66.9(6)
1360.215(12)	4.29(4)
1771.351(16)	15.47(14)
1810.772(17)	0.638(8)
1963.714(12)	0.724(10)
2015.181(16)	3.04(5)
2034.755(13)	7.89(13)
2113.123(10)	0.376(10)
2212.933(18)	0.395(14)
2598.459(13)	17.3(3)
3009.596(7)	1.16(3)
3201.962(16)	3.32(7)
3253.416(15)	8.12(17)
3272.990(15)	1.93(4)
3451.152(17)	0.972(20)
3547.930(60)	0.200(5)

4.4 Photon Flux and Extraction of Integrated Cross Sections

For an extraction of the integrated photon scattering cross section I_S we use the relationship between it and the properties of the nuclear levels. The peak area A_i of a line in an NRF spectrum is related to the physical quantities by

$$A_i = N_{Target} \cdot \int\limits_{T_M} N\left(E_x, E_0, t\right) dt \cdot \varepsilon\left(E_x\right) \cdot I_S^i \cdot W_{eff}^i\left(\theta\right) \cdot \frac{\Delta\Omega}{4\pi} \quad , \tag{27}$$

where N_{Target} is the total number of target nuclei irradiated by the incident photons (taking into account the isotopic enrichment), T_M is the total time of measurements, $N\left(E_x, E_0, t\right)$ is the number of photons crossing the unit of target surface per unit of time, $\varepsilon\left(E_x\right)$ is the detector efficiency, $W_{eff}^i\left(\theta\right)$ is the angular distribution function integrated over the solid angle $\Delta\Omega$ of the detector placed at the angle θ, and the E_x is the energy of the excited level. The number of nuclei in a target is given by

$$N_{Target} = \rho \cdot x \cdot \frac{N_A}{A} \cdot S = \frac{m}{S_{Total}} \cdot \frac{N_A}{A} \cdot S \quad , \tag{28}$$

where ρ is the density, x is the target thickness, S equals the area of the target surface irradiated by the photon flux, N_A is Avogadro's number, A is the mass number, m is the target mass and S_{Total} is the total target area. The determination of the integrated cross section requires a knowledge of the photon flux. The use of calibration targets with areas equal to the one under investigation permits a direct determination of the product of the photon flux $N_\gamma\left(E_x, E_0\right)$ and detector efficiency $\varepsilon\left(E_x\right)$. For $N_\gamma \cdot \varepsilon$ one obtains

$$N_\gamma\left(E_x, E_0\right) \cdot \varepsilon\left(E_x\right) = \frac{A_i}{N_{^{11}B} \cdot I_S^i \cdot W_{eff}^i\left(\theta\right) \cdot \frac{\Delta\Omega}{4\pi}} \quad , \tag{29}$$

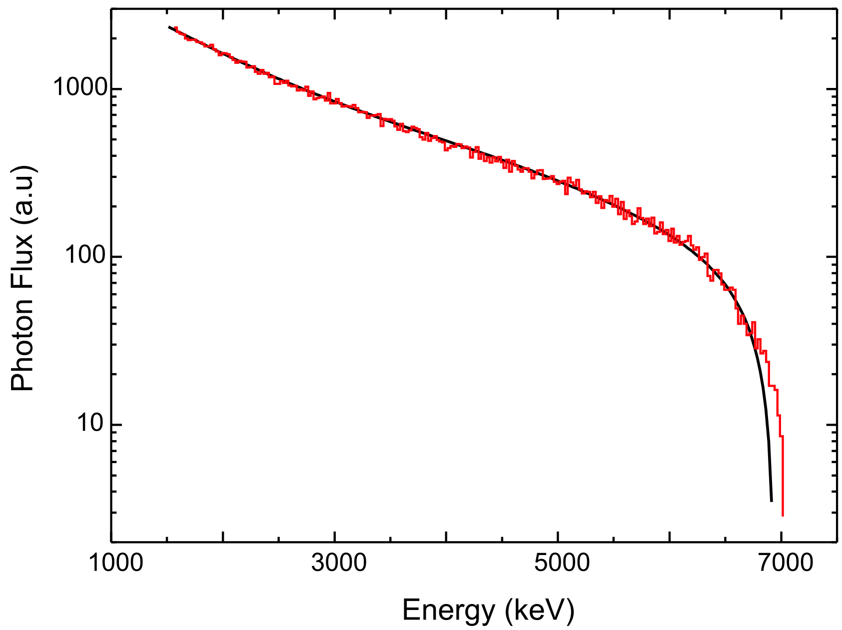

Figure 13: Plot of the relative photon flux between 1 and 7 MeV. A 5^{th} order polynomial function is applied to fit the shape of the photon flux.

where A_i is the peak area of the i-th calibration ^{11}B line. The integrated photon scattering cross sections of the ^{11}B lines used for the determination of $N_\gamma \cdot \varepsilon$ are listed in Tab. 3 [39, 40, 41]. The bremsstrahlung spectrum was simulated [38] using the program GEANT4 with an endpoint energy of 7 MeV. In Fig. 13 the simulated flux is shown together with fit of a polynomial function of 5^{th} degree which provides a good description up to 6.6 MeV. Above, the function significantly underestimates the GEANT4 results. Because GEANT simulations provide only an energy dependence of the flux but not absolute values, one has to normalize these data accordingly to the experimental points of ^{11}B. Figure 14 shows the quantity $N_\gamma \cdot \varepsilon_{abs}$ normalized to the reference ^{11}B levels. Triangles and the solid line mark the products

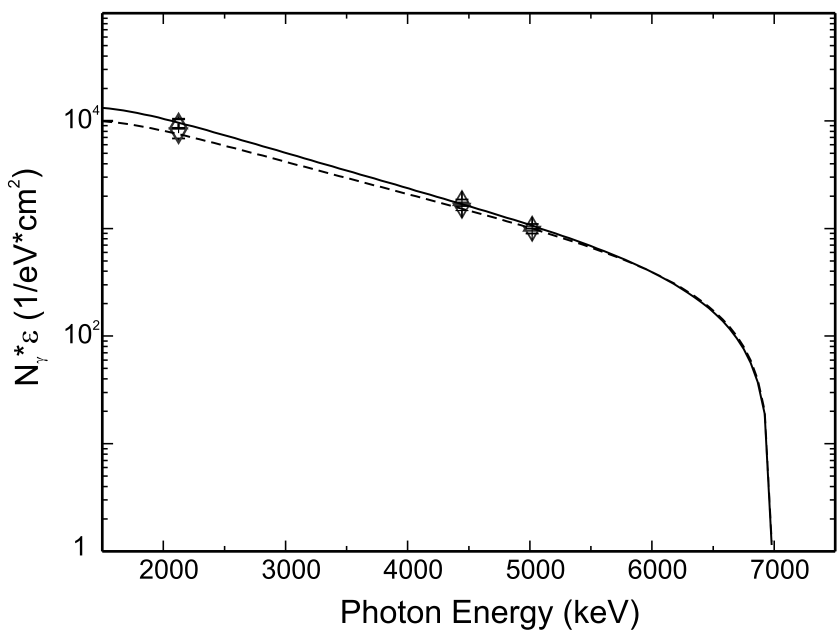

Figure 14: Plot of the fit functions for $N_\gamma \cdot \varepsilon_{abs}$ normalized on ^{11}B lines.

of the $N_\gamma \cdot \varepsilon_{abs}$ and their simulated fit function for 90°, upturned triangles and the dashed line for 130°. The main source of systematic errors in this calibration procedure arises from the possibility of unidentified feeding of the reference levels by inelastic transitions from levels at higher energies. For ^{11}B inelastic transitions are known, and the peak areas have been corrected.

Table 3: Transitions in ^{11}B used for calibration

E_x [keV]	J^π	I_S^0 [10^3 eVfm^2]
2124.69	$\frac{1}{2}^-$	5.1(4)
4444.89	$\frac{5}{2}^-$	16.3(6)
5020.31	$\frac{3}{2}^-$	21.9(8)

Then using Eqs. (12) and (18-20) one can extract the transition widths and the reduced transition probabilities B(E1)↑, B(E2)↑ and B(M1)↑.

4.5 Results

The experimental results for ^{112}Sn are summarized in Tab. 4. The excitation

Table 4: NRF results for ground state transitions in ^{112}Sn.

E_x[keV]	J	$\frac{W(90°)}{W(130°)}$	I_S^i [eVb]	Γ_0^2/Γ[eV]	B(E1)↑ [10^{-3} e^2fm^2]	B(Eλ)↓ [W.u.]
4161.9	1	0.753	29.1 (28)	0.044 (4)	1.75 (14)	0.39 (4)
4726.6	1	0.683	6.9 (14)	0.013 (3)	0.33 (7)	0.08 (2)
5057.0	1	0.826	54.8 (66)	0.122 (13)	2.96 (33)	0.66 (7)
5128.3	1	0.742	19.1 (21)	0.044 (4)	5.02 (36)	1.12 (8)
5246.3	1	0.907	55.7 (47)	0.133 (11)	3.29 (27)	0.73 (6)
5503.0	1	0.697	32.5 (30)	0.086 (8)	1.47 (15)	0.33 (3)
5594.6	1	0.899	15.8 (23)	0.043 (6)	0.70 (11)	0.16 (2)
5646.6	1	0.846	15.5 (25)	0.043 (7)	0.68 (11)	0.19 (3)
5845.6	1	0.601	12.7 (25)	0.038 (7)	0.54 (11)	0.12 (2)
5860.9	1	1.081	53.2 (92)	0.159 (27)	2.26 (40)	0.50 (9)
5883.7	1	1.102	33.1 (55)	0.100 (16)	1.41 (24)	0.31 (5)
5924.6	1	0.96	36.8 (39)	0.112 (12)	1.54 (18)	0.34 (4)
5977.1	1	0.657	40.9 (47)	0.127 (14)	1.70 (21)	0.38 (5)
6005.0	1	0.881	78.01 (67)	0.244 (21)	3.22 (31)	0.72 (7)
6058.9	1	0.626	148 (14)	0.470 (44)	6.06 (63)	1.35 (14)

Table 4: (Continued)

E_γ[keV]	J	$\frac{W(90°)}{W(130°)}$	I_S^i [eVb]	Γ_0^2/Γ[eV]	B(E1)↑ [10^{-3} e^2fm^2]	B(Eλ)↓ [W.u.]
6080.5	1	0.785	22.9 (37)	0.073 (12)	0.94 (16)	0.21 (4)
6096.2	1	0.585	88.7 (72)	0.286 (23)	3.61 (29)	0.80 (7)
6128.4	1	0.710	35.3 (41)	0.115 (13)	1.43 (18)	0.32 (4)
6150.1	1	0.559	82.9 (86)	0.272 (28)	3.36 (38)	0.75 (8)
6168.1	1	0.657	21.5 (41)	0.071 (14)	0.87 (17)	0.19 (4)
6198.6	1	0.648	53.7 (55)	0.179 (18)	2.16 (24)	0.48 (5)
6224.7	1	0.727	93.6 (76)	0.315 (26)	3.74 (34)	0.83 (8)
6245.7	1	0.667	50.7 (51)	0.172 (17)	2.02 (22)	0.45 (5)
6258.1	1	0.681	38.1 (51)	0.129 (17)	1.51 (21)	0.34 (5)
6273.1	1	0.623	64.4 (61)	0.220 (21)	2.55 (26)	0.57 (6)
6313.2	1	0.582	51.7 (56)	0.179 (19)	2.04 (24)	0.45 (5)
6387.7	1	0.659	187 (13)	0.664 (47)	7.29 (60)	1.62 (13)
6404.3	1	0.785	457 (36)	1.626 (127)	17.8 (16)	3.95 (35)
6425.8	1	0.684	24.5 (45)	0.088 (16)	0.95 (18)	0.21 (4)
6432.8	1	0.698	41.7 (69)	0.150 (26)	1.61 (28)	0.36 (6)
6438.0	1	0.623	42.9 (71)	0.154 (26)	1.66 (28)	0.37 (6)
6450.7	1	0.760	31.3 (50)	0.113 (19)	1.21 (20)	0.27 (4)
6521.2	1	0.507	83.8 (92)	0.309 (34)	3.20 (35)	0.70 (12)
6601.9	1	0.507	45.8 (90)	0.173 (34)	1.73 (36)	0.38 (17)
6714.8	1	0.735	39.7 (84)	0.156 (33)	1.47 (31)	0.33 (7)
6734.2	1	0.547	36.7 (93)	0.145 (37)	1.36 (35)	0.30 (8)
6822.9	1	0.922	88.8 (17)	0.347 (76)	3.13 (68)	0.69 (16)

energy E_x and tentative spin J of each excited level are given. Furthermore, the elastic transition strengths Γ_0^2/Γ and the corresponding reduced transition probabilities B(E1)$\uparrow$ are also listed. Calculations of the B(E1) values are based on the assumption that all observed dipole transitions have electric character. From some levels decays to the first 2^+ state were observed. The

Table 5: Characteristics of the inelastic transitions from excited levels to the first 2^+ state.

E_x [keV]	b_i [%]	Γ_i [meV]	B(E1)$\downarrow$ [10^{-3} e^2fm^2]
5057.0	9	12.8 (52)	0.13 (5)
5128.0	82	1039 (148)	10.3 (15)
5246.0	17	32.9 (58)	0.30 (5)
5646.0	19	12.1 (41)	0.08 (3)

branching ratios to the 2_1^+ for these levels b_i, transition widths Γ_i and B(E1) strengths for $1^- \rightarrow 2^+$ transitions are given in the Tab. 5.
The B(E1)$\uparrow$ strength distribution of the ^{112}Sn nuclide is shown on Fig. 15. Up to now most of these transitions were unknown. The strongest lines are located between energies from 6 MeV to 7 MeV and may be interpreted as part of the Pygmy dipole resonance. The comparison of the results obtained at two different endpoint energies of 5.5 MeV and 7 MeV is shown in Tab. 6. The observed 2^+ states exhibit large differences in the integrated cross sections and transition strengths, and that is the signature of the strong feeding, also seen in Fig. 11. Comparing the transition strength populating the 2_1^+ state at an endpoint energy of 5.5 MeV with data given by Ref. [21], it is concluded that strong feeding is present too. In the 7 MeV the transition

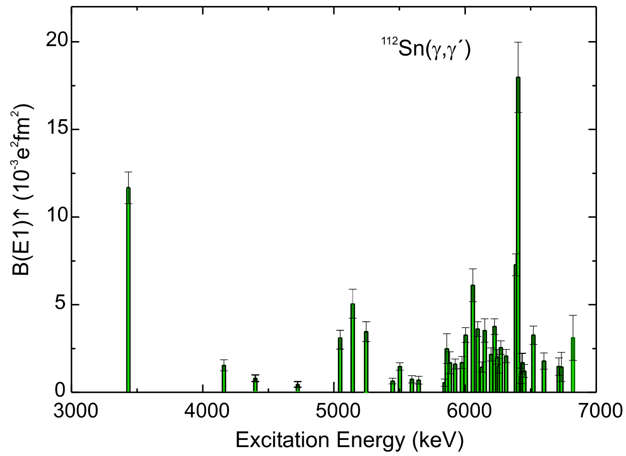

Figure 15: Distribution of the E1 strength in ^{112}Sn deduced from the (γ, γ') reaction at an endpoint energy E_0=7 MeV.

Table 6: Comparison of the results obtained at E_0 =5.5 MeV and 7 MeV.

E_γ[keV]	J^π	Γ_0^2/Γ [meV]^a	Γ_0^2/Γ [meV]^b	$B(E\lambda)\uparrow$ [e^{2}fm$^{2\lambda}$]^a	$B(E\lambda)\uparrow$ [e^{2}fm$^{2\lambda}$]^b
1256.6	2^+	2.9 (8)	7.8 (6)	5721 (1540)	15533 (1273)
3089.6	2^+	12.4 (20)	14.7 (17)	273 (44)	326 (37)
3433.7	1^-	163 (13)	162 (9)	0.0116 (9)	0.0115 (6)
4161.9	$1^{(-)}$	35.9 (70)	43.7 (42)	0.0014 (3)	0.0017 (2)
5057.1	$1^{(-)}$	85.6 (17)	122 (15)	0.0019 (3)	0.0030 (3)

$^a E_0$=5.5 MeV
$^b E_0$=7 MeV

strength of the 1^- state at 3434 keV, which was interpreted as two-phonon state by Ref. [36] shows, deduced at the two endpoint energies agrees within error bars. The same holds for the transition to the level at 4162 keV. The state at 5057 keV is fed significantly which is also seen in Fig. 11.

5 Discussion

The appearance of low-energy electric dipole strength is a genuine feature of neutron-rich nuclei, seen recently in stable nuclei with small [42, 43] and moderate [9] neutron excess. The gross properties of this Pygmy dipole resonance are the energy centroid and the total reduced transition probability $\sum$B(E1). They should give the first access to the nature of the PDR, e.g. a possible relation with the neutron skin thickness.

The comparison of the B(E1) strength measured in the present experiment with that obtained in earlier experiments on the 116 and 124 tin isotopes carried out by the Gent group [18] is shown in Fig. 16. The comparison was limited up to an excitation energy of 6.5 MeV. The extracted summed reduced B(E1) transition probabilities and their centroids in the three experiments are 0.089 e^2fm^2 and 6.14 MeV, 0.122 e^2fm^2 and 6.18 MeV, 0.111 e^2fm^2 and 6.3 MeV for ^{112}Sn, ^{116}Sn, ^{124}Sn, respectively. Comparing results for ^{116,124}Sn with an endpoint energy of 10 MeV one can estimate the order of the missing strength for ^{112}Sn at higher excitation energies. Approximately half of $\sum$B(E1) is missing. The additional data for ^{112}Sn obtained at an endpoint energy of 9.5 MeV should clarify this part.

Results based on calculations in a relativistic quasiparticle random phase approximation (RQRPA) in the canonical single-nucleon basis of the relativistic Hartree-Bogoliubov (RHB) model [17] show a smooth increase of $\sum$B(E1) strength and a smooth decreasing of Pygmy dipole resonance centroid in the region of stable tin isotopes. They predict in ^{112}Sn the existence of a resonance with centroid energy at 9.4 MeV and total B(E1) strength of

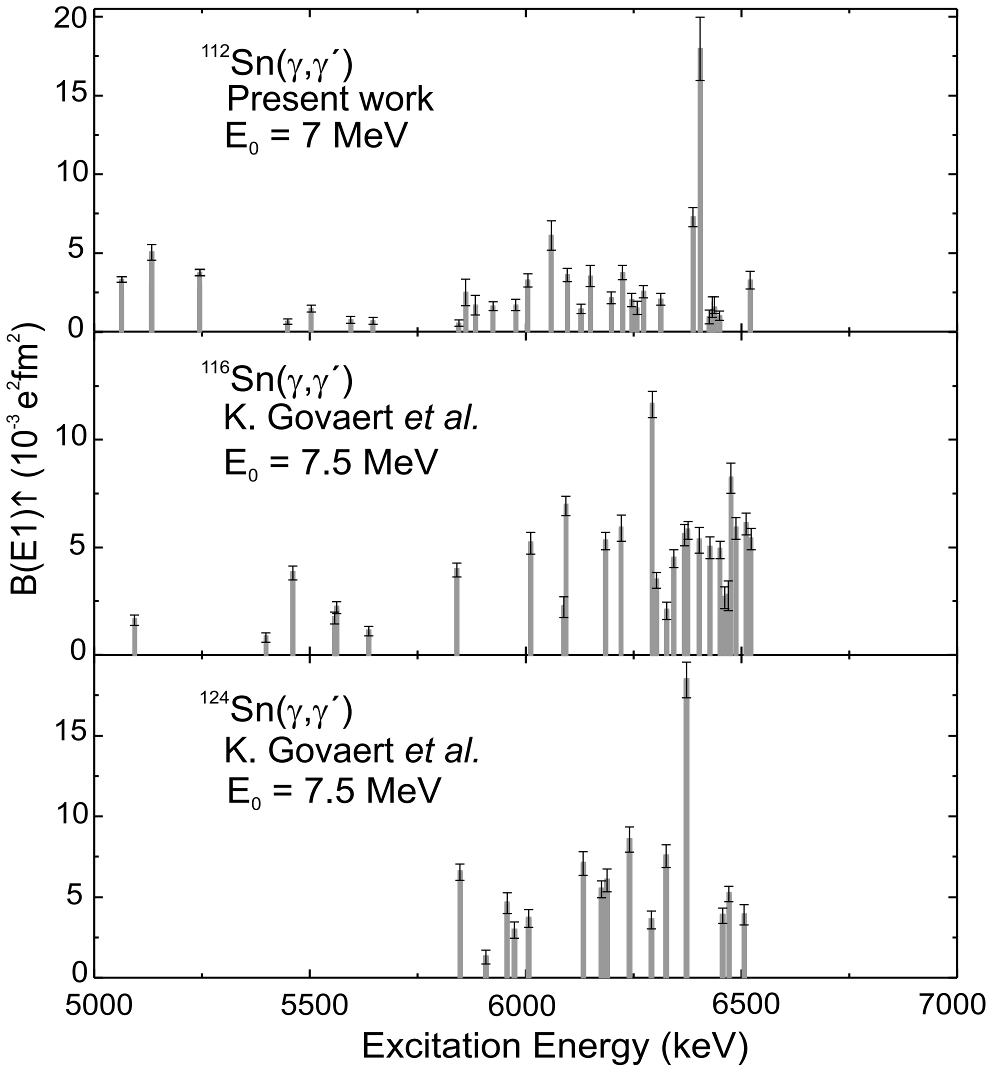

Figure 16: Comparison of the reduced transition probabilities in ^{112}Sn (upper part) from the present experiment with the ones obtained in ^{116}Sn (middle part) and ^{124}Sn (lower part) from Ref. [18] for $E_x \leq 6.5$ MeV.

$0.285\ e^2 fm^2$. Figure 17 shows the comparison of such theory calculations for tin isotopes in the mass range of A = 100-132 with experimental data obtained for 112, 116 and 124 tin isotopes where the upper panel displays the case of $\sum$B(E1) while the down panel the case of resonance centroid. A realistic comparison between experiment and the model prediction has to await the final analysis of the B(E1) strength in ^{112}Sn for bremsstrahlung endpoint energy up to particle threshold which is presently underway [35].

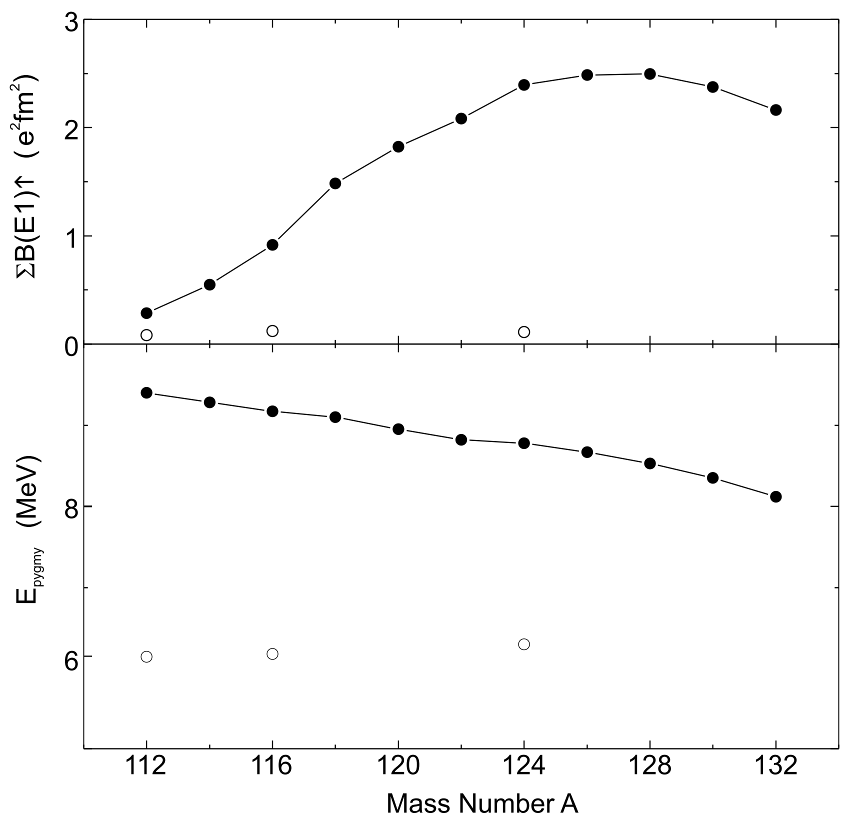

Figure 17: Comparison of the theoretical values of ΣB(E1) strengths and PDR centroids [17, 44] (full circles) for the chain of tin isotopes with experimental values (open circles).

6 Concluding Remarks

By means of resonant scattering of real photon of an endpoint energy of 5.5 MeV and 7 MeV a study of the dipole strength distribution in the semi-magic even-even ^{112}Sn nucleus has been performed at the S-DALINAC up to an excitation energy of 7 MeV. The experiment aimed at the search for the Pygmy dipole resonance, being predicted by different models at different energies with difference strength. Below the Giant dipole resonance a detailed picture of the fine structure of the dipole strength has been obtained. Besides the well-known 2^+ states and the $[2^+ \times 3^-]$ 1^- two-phonon state, more than 30 new dipole ground state transitions in ^{112}Sn were observed. The excitation energies and the ground state transition width of the corresponding levels have been determined. The observed dipole strength distribution displays a clear concentration at energies between 6 and 7 MeV with a total strength of 93.0(24) 10^{-3} $e^2 fm^2$, under the assumption that all observed dipole transitions have E1 character. However, before a final comparison with model calculations can be performed, a complete analysis of data taken at an even higher endpoint energy of 9.5 MeV has to be performed.

References

[1] B.L. Berman, S.C. Fultz, Rev. Mod. Phys. 47, 713 (1975).

[2] A. Bohr, B. Mottelson, *Nuclear Structure*, Vols.1 and 2, (World Scientific, Singapore 1998).

[3] W.Andrejtscheff, C. Kohstall, P. von Brentano, C. Fransen, U. Kneissl, N. Pietralla, H.H. Pitz, Phys. Lett. B 506, 239 (2001).

[4] P.O. Lipas, Nucl. Phys A 573, 231 (1994).

[5] G.A. Bartholomew, E.D. Earle, A.J. Ferguson, J.W. Knowles, M.A. Lone, Adv. Nucl. Phys. 7, 229 (1972).

[6] E.B. Balbutsev, I.V. Molodtsova, A.V. Unzhakova, Europhys. Lett. 26, 499 (1994).

[7] T. Hartmann, J. Enders, P. Mohr, K. Vogt, S. Volz, A. Zilges, Phys. Rev. Lett. 85, 274 (2000).

[8] A. Zilges, S. Volz, M. Babilon, T. Hartmann, P. Mohr, K. Vogt, Phys. Lett. B 542, 43 (2002).

[9] N. Ryezayeva, T. Hartmann, Y. Kalmykov, H. Lenske, P. von Neumann-Cosel, V.Yu. Ponomarev, A. Richter, A. Shevchenko, S. Volz, J. Wambach, Phys. Rev. Lett. 89, 27 (2002).

[10] N. Ryezayeva, B.A. Brown, Y. Kalmykov, H. Lenske, P. von Neumann-Cosel, V.Yu. Ponomarev, A. Richter, A. Shevchenko, J. Wambach, Nucl. Phys. A, submitted.

[11] F.R. Metzger, Resonance Fluorescence in Nuclei, Progr. Nucl. Phys. 7, 54 (1959).

[12] A. Leistenschneider, T. Aumann, K. Boretzky, D. Cortina, J. Cub, U.D. Pramanik, W. Dostal, Th.W. Elze, H. Emling, H. Geissel, A. Grünschloss, M. Hellstrüm, R. Holzmann, S. Ilievski, N. Iwasa, M. Kaspar, A. Kleinbohl, J.V. Kratz, R. Kulessa, Y. Leifels, E. Lubkiewicz, G. Münzenberg, P. Reiter, M. Rejmund, C. Scheidenberger, C. Schlegel, H. Simon, J. Stroth, K. Sümmerer, E. Wajda, W. Walus, S. Wan, Phys. Rev. Lett. 86, 5442 (2001).

[13] E. Tryggestad, T. Baumann, P. Heckman, M. Thoennessen, T. Aumann, D. Bazin, Y. Blumenfeld, J.R. Beene, T.A. Lewis, D.C. Radford, D. Shapira, R.L. Varner, M. Chartier, M.L. Halbert, J.F. Liang, Phys. Rev. C 67, 064309 (2003).

[14] R. Palit, P. Adrich, T. Aumann, K. Boretzky, D. Cortina, U. Datta Pramanik, Th.W. Elze, H. Emling, M. Fallot, H. Geissel, M. Hellström, K.L. Jones, L.H. Khiem, J.V. Kratz, R. Kulessa, Y. Leifels, A. Leistenschneider, G. Münzenberg, C. Nociforo, P. Reiter, H. Simon, K. Sümmerer, W.Walus, Nucl. Phys. A 731, 235 (2004).

[15] N. Tsoneva, H. Lenske, Ch. Stoyanov, Nucl. Phys. A 731, 273 (2004).

[16] N. Tsoneva, H. Lenske, Ch. Stoyanov, Phys. Lett. B 586, 213 (2004).

[17] N. Paar, P. Ring, T. Nikšić, D. Vretenar Phys. Rev. C 67, 034312 (2003).

[18] K. Govaert, F. Bauwens, J. Bryssink, D. De Frenne, E. Jacobs, W. Mondelaers, Phys. Rev. C 57, 2229 (1998).

[19] J. Bryssinck, L. Govor, V.Yu. Ponomarev, F. Bauwens, O. Beck, D. Belic, P. von Brentano, D. De Frenne, T. Eckert, C. Fransen, K. Govaert, R.-D. Herzberg, E. Jacobs, U. Kniessl, H. Maser, A. Nord, N. Pietralla, H.H. Pitz, V. Werner, Phys. Rev C 61, 024309 (2000).

[20] J. Bryssinck, L. Govor, D. Belic, F. Bauwens, O. Beck, P. von Brentano, D. De Frenne, T. Eckert, C. Fransen, K. Govaert, R.-D. Herzberg, E. Jacobs, U. Kniessl, H. Maser, A. Nord, N. Pietralla, H.H. Pitz, V.Yu. Ponomarev, V. Werner, Phys. Rev. C 59, 1930 (1999).

[21] Nuclear Data Sheets; //www.nndc.bnl.gov/.

[22] U.Kneissl, H.H. Pitz, A. Zilges, Prog. Part. Nucl. Phys. 37, 349 (1996).

[23] J. Enders, P. von Brentano, J. Eberth, A. Fitzler, C. Fransen, R.-D. Herzberg, H. Kaiser, L. Käubler, P. von Neumann-Cosel, N. Pietralla, V.Yu. Ponomarev, A. Richter, R. Schwenger, I. Wiedenhöver, Nucl. Phys. A 724, 243 (2003).

[24] H.A. Bethe and G. Placzek, Phys. Rev 51, 450 (1937).

[25] H. Frauenfelder, R. M. Steffen, Angular Correlation Methods in Gamma-Ray Spectroscopy, in: *Alpha-, Beta- and Gamma-Ray Spectroscopy*, ed. K. Siegbahn (North-Holland, Amsterdam, 1965).

[26] A. Richter, Proceeding of the Fifth European Particle Accelerator Conference, ed. S. Meyers et al., (IOP Publishing, Bristol, 1996) 110.

[27] P. Mohr, J. Enders, T. Hartmann, H. Kaiser, D. Schiesser, S. Schmitt, S. Volz, F. Wissel, A. Zilges, Nucl. Instr. Meth. A 423, 480 (1999).

[28] S. Volz, Diploma thesis, TU Darmstadt, (2001).

[29] G.F. Knoll, *Radiation Detection and Measurement*, 2^{nd} Ed. (Wiley, New York, 1989).

[30] D. Savran, Diploma thesis, TU Darmstadt, (2004).

[31] C. Hutter, Diploma thesis, TU Darmstadt, (2001).

[32] K. Okajama, K. Takami, K. Ueda, F. Kawagushi, Rev. Sci. Instrum. 53, 1285 (1982).

[33] W.R. Leo, Techniques for Nuclear and Particle Physics Experiments, Springer-Verlag, Berlin, (1994).

[34] T. Hartmann, Dissirtation, TU Darmstadt, (2003).

[35] B. Özel, Dissirtation, University of Cukurova, in preparation.

[36] I. Pysmenetska, Diploma thesis, TU Darmstadt (2004).

[37] I. Bauske, J.M. Arias, P. von Brentano, A. Frank, H. Friedrichs, R.D. Heil, R.-D. Herzberg, F. Hoyler, P. van Isacker, U. Kneissl, J. Margraf, H.H. Pitz, C. Wesselborg, A. Zilges, Phys. Rev. Lett. 79, 2010 (1997).

[38] S. Volz, private communication

[39] R. Moreh, W.C. Sellyey, R. Vodhanel, Phys.Rev. C 22, 1820 (1980).

[40] F. Ajzenberg-Selove, Nucl. Phys. A 506, 1 (1990).

[41] F. Ajzenberg-Selove, Nucl. Phys. A 433, 1 (1985).

[42] T. Hartmann, M. Babilon, S. Kamerdzhiev, E. Litvinova, D. Savran, S. Volz, A. Zilges, Phys. Rev. Lett 93, 192501 (2004).

[43] A. Zilges, S. Volz, M. Babilon, T. Hartmann, P. Mohr, K. Vogt, Phys. Lett. B 542, 43 (2002).

[44] N. Paar, private communication.

Acknowledgements

At this place I would like to thank all persons who have contributed to the success of this work.

On the first place I would like to sincerely thank *Professor Dr. Dr. h. c. mult. Achim Richter* for the given opportunity to work on such an exciting topic under his supervision and to sense the climate of constructive team work in a modern scientific laboratory.

Further on I would like to thank *Privatdozent Dr. Peter von Neumann-Cosel* for the numerous useful discussions during the realization of this diploma thesis and for valuable remarks that he has made during the reading of this thesis, the significance of which it is difficult to overestimate.

I address my heartfelt gratitude to *Dr. Harald Genz* for his every day help, care and support.

I also would like to thank *Professor Joachim Enders* for numerous discussions during the work.

I am also grateful to my twin-sister *Yuliya* for care and support during our staying in Germany. Thank you very much!

I would like to thank especially *Dipl.-Phys. Natalya Ryezayeva* for her numerous useful discussions and advices.

I would like to express my gratitude also to *Dr. Sergiy Khodyachykh, Maksym Chernykh, Olena Yevetska, Oleksiy Burda, Artem Shevchenko, Dr. Yaroslav Kalmykov, Dr. Mykhaylo Gopych* for their support and numerous significant advices. Thank you very much!

I am also grateful to *Dipl.-Phys. Stephan Volz* for all given information and his help during my work.

I am very grateful to TU Darmstadt and Institute für Kernphysik for their financial support.

I would like to express my gratitude to *E.S. Shmatko, V.D. Afanas'ev, A.F. Shchus* and Chair of the Experimental Nuclear Physics of the Karazin Kharkiv National University (Ukraine) for the time they have spent for my education.

Finally, my heartful gratitude to my family - my mother *Margarita* and my elder sister *Olena*, and to my friends in Ukraine. Your thoughts and your care were supporting me very much during my study in the Karazin Kharkov University and during my stay in Darmstadt.